nature physics

Article

https://doi.org/10.1038/s41567-022-01777-8

Enhanced metrology at the critical point of a many-body Rydberg atomic system

Received: 19 November 2021

Accepted: 1 September 2022

Published online: 17 October 2022

Check for updates

Dong-Sheng Ding[1,2,3,7], Zong-Kai Liu[1,2,3,7], Bao-Sen Shi[1,2,3], Guang-Can Guo[1,2,3], Klaus Mølmer[4,5] and Charles S. Adams[6]

Interacting many-body systems display enhanced sensitivity close to critical transition points due to diverging quantum fluctuations. This criticality-based enhancement has been suggested as a potential resource for applications in precision metrology. Here we demonstrate many-body critical enhanced metrology for the sensing of external microwave electric fields in a non-equilibrium Rydberg atomic gas. We show that small variations in external driving lead to a large variation in the population of Rydberg states around criticality and to a notable change in the optical transmission signal. For continuous optical transmission at the critical point, we quantify the enhanced sensitivity extracting the Fisher information, which shows a three orders of magnitude increase due to many-body effects compared with single-particle systems. These results demonstrate that critical properties of many-body systems are promising resources for sensing and metrology applications.

Ensembles of well-controlled neutral atoms are ideal systems to explore many-body physics[1–4]. In particular, the controllable interactions among highly excited Rydberg atoms hold promise for studies of quantum information and many-body physics[5–7]. Benefiting from the large interaction volume of Rydberg atoms, a small change in the Rydberg state population can induce a global macroscopic phase transition between non-interacting and interacting phases[8]. Laser-induced density-dependent energy shifts of Rydberg states offer a convenient platform to directly observe non-equilibrium phase transitions and bistability[7,9–12], and to study dynamical analogues of forest fire[8] and epidemic spread[13,14]. In contrast to other optically bistable systems[15–19], Rydberg ensemble experiments can be performed without the need of optical cavity feedback and cryogenic temperatures.

Exploring the non-equilibrium dynamics of the Rydberg system under external fields is intriguing. The emergent thermodynamic and spectroscopic properties of a many-body system of interacting Rydberg atoms present open questions both in theory[11,20–23] and experiments[7,8]. Due to the large dipole moment, the Rydberg atoms are highly sensitive to system noise and external electric fields[24–29]. Most dramatically, the macroscopic change in optical response near a critical point[8,12] presents a resource for increased metrological sensitivity[30–40]. Accompanying the divergent susceptibility near the critical point, optical probing of the system is highly sensitive to small variations in physical parameters. Critical systems may, thus, display sensing errors with a generic scaling of $\sim 1/\sqrt{N^{\gamma} t^{\lambda}}$, where $\gamma, \lambda > 1$ (refs. [37,41,42]), N is the number of atoms and t is the measurement time.

In this Article, we demonstrate how Rydberg criticality provides a method for the high-sensitivity probing of external parameters. We exploit the extreme sensitivity of optical transmission at the critical point to probe external microwave (MW) fields. Due to the critical slowing down near phase transitions, we need to take into account how the system dynamics do not adiabatically follow the stationary state, but rather smooths the system response. This leads to a non-integer power dependence of the Fisher information (FI) on the duration of the detuning scans. The behaviour around criticality is observed to

[1]CAS Key Laboratory of Quantum Information, University of Science and Technology of China, Hefei, China. [2]CAS Center for Excellence in Quantum Information and Quantum Physics, University of Science and Technology of China, Hefei, China. [3]Hefei National Laboratory, University of Science and Technology of China, Hefei, China. [4]Aarhus Institute of Advanced Studies, Aarhus University, Aarhus C, Denmark. [5]Center for Complex Quantum Systems, Department of Physics and Astronomy, Aarhus University, Aarhus C, Denmark. [6]Department of Physics, Durham University, Durham, UK. [7]These authors contributed equally: Dong-Sheng Ding, Zong-Kai Liu. e-mail: dds@ustc.edu.cn; drshi@ustc.edu.cn; moelmer@phys.au.dk; c.s.adams@durham.ac.uk

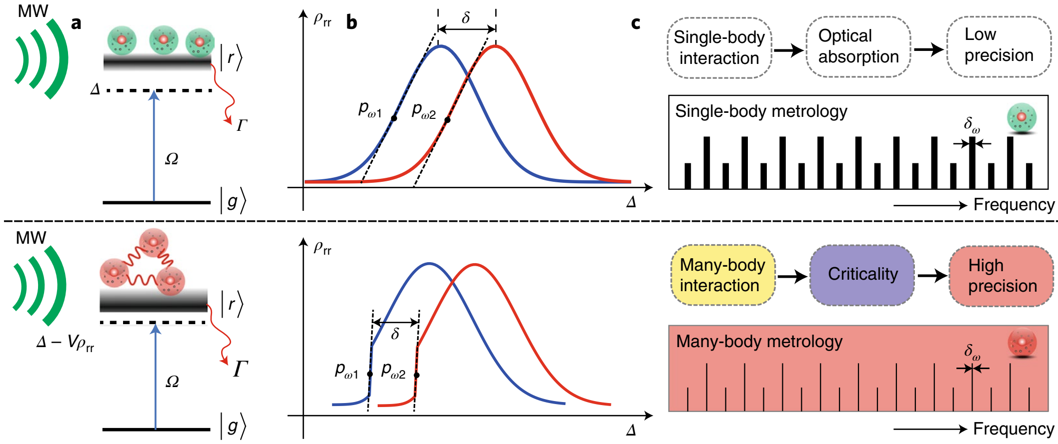

Fig. 1 | Principle of single-body (top) (many-body (bottom)) Rydberg metrology. a, Energy diagram for a two-level atom model, showing the ground state $|g\rangle$ and Rydberg state $|r\rangle$ with spontaneous radiation rate Γ. The atoms are driven from the ground state to the Rydberg state by a laser with Rabi frequency Ω and detuning Δ. They are also exposed to an MW field with electric-field component E_{mw}. In the many-body case, the Rydberg resonance is modified by the many-body interaction strength, namely, $V = C_6/r^6$ (where C_6 is the van der Waals coefficient and r is the distance between Rydberg atoms), as well as the population of the Rydberg atoms ρ_{rr} (Methods). **b**, The blue and red curves represent the spectrum with and without the external MW field, which induces a shift δ. The measurement sensitivity is the highest when the derivative $d\rho_{rr}/d\Delta$ is the maximum, as indicated by points $p_{\omega1}$ and $p_{\omega2}$. The steeper slope near the critical point in the many-body case (bottom) results in enhanced measurement sensitivity. **c**, Many-body advantage corresponds to a metrological ruler with thinner tick marks $\delta\omega$ than in the single-body case. The transmission spectra are shifted by an external electrical field forming a ruler with unfixed ticks.

enhance the FI by a factor of up to more than 10^3 compared with a non-interacting ensemble.

Results

Many-body metrology model

We consider a model of N interacting two-level atoms with a ground state $|g\rangle$ and Rydberg state $|r\rangle$ (with decay rate Γ) (Fig. 1a). A laser couples these atoms with Rabi frequency Ω and detuning Δ. We derive the Rydberg population ρ_{rr} via mean-field approximation (that is, $\Delta \to \Delta - V\rho_{rr}$, where V is the average many-body interaction strength from dipole interaction or ion collisions) and δ is the external-field-induced frequency shift on Rydberg state $|r\rangle$ (Methods):

$$\rho_{rr} = \frac{\Omega^2}{4(\Delta - V\rho_{rr})^2 + 2\Omega^2 + \Gamma^2}. \quad (1)$$

Due to the interaction, the spectrum has a population-dependent shift $V\rho_{rr}$, thus inducing a steep edge of ρ_{rr} with a maximum derivative

$$\left.\frac{d\rho_{rr}}{d\Delta}\right|_{\Delta=\Delta_c} = \frac{1}{V + \sqrt{(\Gamma^2 + 2\Omega^2)/3\rho_{rr}^2}}, \quad (2)$$

where Δ_c corresponds to the detuning at which the derivative gets its maximum. We note that $d\rho_{rr}/d\Delta$ increases due to the interaction strength V (here $V < 0$) (Methods). The derivative $d\rho_{rr}/d\Delta$ diverges at the system's critical point[8], exhibiting a method of high-precision measurement[30–36]. A measurement is realized by detecting the transmission of an optical probe field. When applying external fields (such as the electric component of external MW fields), the measurement precision is limited by the maximum slope of the Rydberg resonance. This is indicated by the points $p_{\omega1}$ ($p_{\omega2}$) (Fig. 1b). Compared with the non-interacting case (Fig. 1b, top), the slope in the vicinity of the critical point (Fig. 1b, bottom) is notably enhanced. For metrology applications, the sensitivity of the many-body case is enhanced by the ratio

$$\beta = \left.\frac{d\rho_{rr}}{d\Delta}\right|_{V\neq0} / \left.\frac{d\rho_{rr}}{d\Delta}\right|_{V=0}. \quad (3)$$

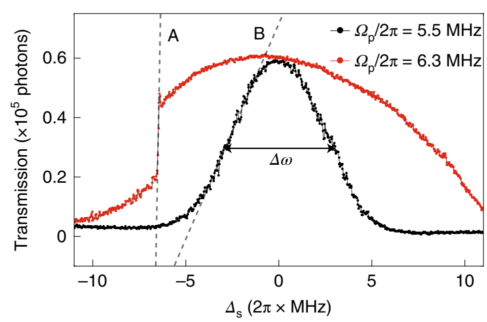

Fig. 2 | Optical transmission spectra with and without phase transition. Transmission spectra with (red) and without (black) the phase transition. The dashed lines A and B show the maximum slopes near the half-transmission. Here $\Delta\omega/2\pi \approx 6$ MHz shows the bandwidth of the transmission spectrum without interactions. The photon counts are given for a measurement time $t = 20$ μs for a detuning interval of $2\pi \times 0.036$ MHz.

In Fig. 1c, we illustrate how this many-body enhancement is like having a new ruler with much finer markings.

The measurement sensitivity is determined by the variation in the transmission signal around the critical point and the photon-counting noise in the measurement record. By exploring the linear slope of transmission in a narrow interval around the critical point, the sensitivity can be expressed in terms of FI[43,44] as

$$F(\Delta) = \frac{\overline{\mu}'(\Delta)^2}{\mathrm{Var}(\mu)}, \quad (4)$$

where Δ is the parameter that we want to determine and $\overline{\mu}$ represents the mean value of the difference in photon numbers accumulated in fixed time intervals by a differential detector exposed to a reference beam and a beam passing through the atomic cloud. Var(μ) is the variance of the differential signal, that is, the sum of the variances of the two separate and independent counting signals. Note that equation (4)

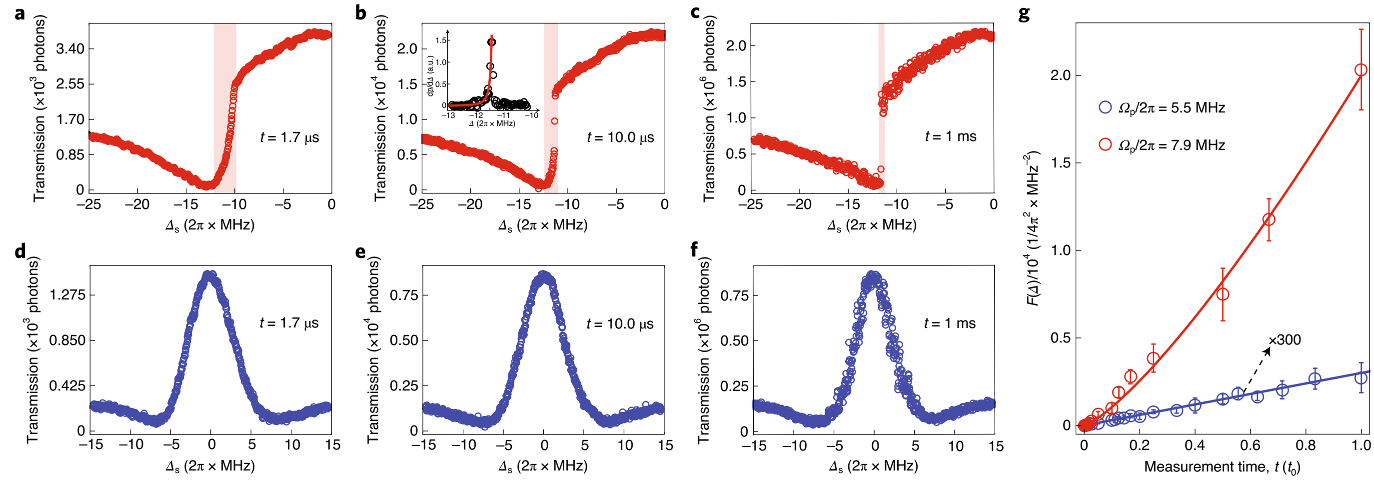

Fig. 3 | Transmission spectra and associated FI. a–c, Transmission spectra across the phase transition (shaded regions), obtained in a total measurement time of 1.7 μs (**a**), 10.0 μs (**b**) and 1 ms (**c**). The inset in **b** shows the corresponding derivative $d\bar{\mu}/d\Delta_s$. **d–f**, Trivial spectra (without phase transition) for the same measurement times of 1.7 μs (**d**), 10.0 μs (**e**) and 1 ms (**f**). **g**, FI associated with the determination of the steepest point on the transmission curves for different values of t (note that the FI for the non-interacting case is manually magnified by a factor of 300). The red and blue curves are fitted by the function $F = A(t/t_0)^\lambda$, where the fit parameters are given in the main text. In this process, the red data in **g** are obtained from the maximum of $F(\Delta)|_{\Delta_s=\Delta_c} = (d\bar{\mu}/d\Delta_s)^2/\mathrm{Var}(\mu)$, whereas for the blue data in **g**, the FI at the critical point is obtained by considering 30 data points around Δ_c in **d–f** to reduce the fluctuations from the instability of the laser power and cell temperature. The error bars determined in **g** are statistics from the three repeated experiments and presented as mean values ± standard deviation.

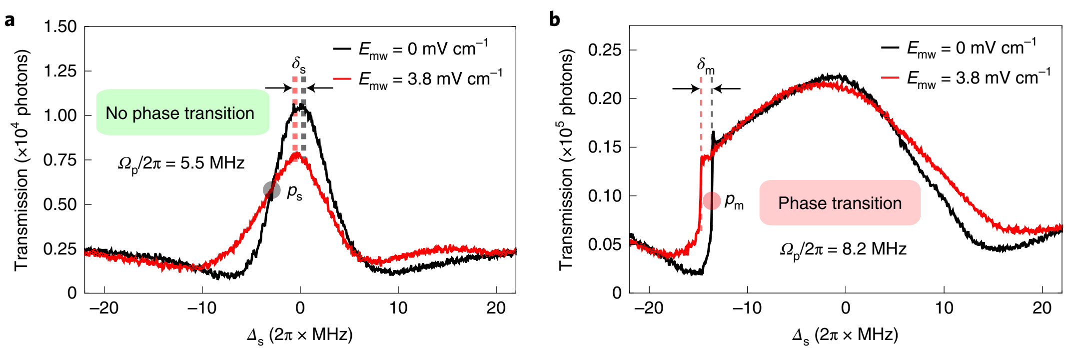

Fig. 4 | Change in transmission spectra by application of MW fields. a, Transmission spectra under the field amplitude $E_{mw} = 0$ mV cm^{-1} (black) and $E_{mw} = 3.8$ mV cm^{-1} (red) with probe Rabi frequency $\Omega_p = 2\pi \times 5.5$ MHz below the critical value $\Omega_{p,c} = 2$ for the phase transition. **b**, Transmission spectra under the field amplitude $E_{mw} = 0$ mV cm^{-1} (black) and $E_{mw} = 3.8$ mV cm^{-1} (red) with probe Rabi frequency $\Omega_p = 2\pi \times 8.2$ MHz, above the critical value for phase transition. In these two cases, the frequency of applied MW field is set as $2\pi \times 16.68$ GHz. The big circular points p_s and p_m (grey and red in **a** and **b**, respectively) correspond to the position of the steepest slope. The direction of scanning Δ_c is from red detuning towards the blue detuning. Here Δ_s is swept from $-2\pi \times 30$ to $-2\pi \times 24$ MHz with sweep rate $\upsilon_s = 2\pi \times 0.0055$ MHz μs^{-1}.

expresses the usual signal-to-noise ratio, and the Cramér–Rao bound, that is,

$$\delta\Delta \geq \frac{1}{\sqrt{F(\Delta)}}, \tag{5}$$

yields the usual estimation error for the counting signal.

It is important to emphasize that FI refers to the actual counting signals. Although a detector may output a photon rate in counts per second, we must independently assess or estimate the variance of the signal for the time duration of the measurement. We explore experiments with different durations and we shall, thus, present the actual counts in the given time intervals and their variance to obtain the proper assessment of metrological sensitivity. We shall also observe that during a frequency scan in finite time, the non-interacting (interacting) atomic system does (does not) attain its stationary state. This leads to a linear (nonlinear) dependence of FI on the measurement time.

Measured derivative and FI

For the experiment, we employ two-photon excitation with a probe beam and a coupling laser beam with Rabi frequencies (detuning) Ω_p (Δ_s) and Ω_c (Δ_c). We measure the transmission spectra (Fig. 2a). The transmission depends on Ω_p, and we can prepare the system with and without phase transition, that is, $\Omega_p < \Omega_{p,c}$ and $\Omega_p > \Omega_{p,c}$, where $\Omega_{p,c}/2\pi = 5.6$ MHz is the threshold Rabi frequency of the probe field. Our system displays a second-order dynamical phase transition between two stationary states with different excitation densities[21]. The two spectra display the main distinct character of the transmission of a non-interacting system (Fig. 2a, black curve) and an interacting many-body system (Fig. 2a, red curve). The derivative $d\mu/d\Delta_s$ of the transmission is very large at the phase transition point Δ_c of the red curve (Fig. 2a), whereas it explores a weaker, finite maximum near the half-maximum of the black curve (Fig. 2a).

In the experiment, we sweep detuning Δ_s and observe the transmission at each Δ_s. As explained above, the FI is not only governed by the

https://doi.org/10.1038/s41567-022-01777-8

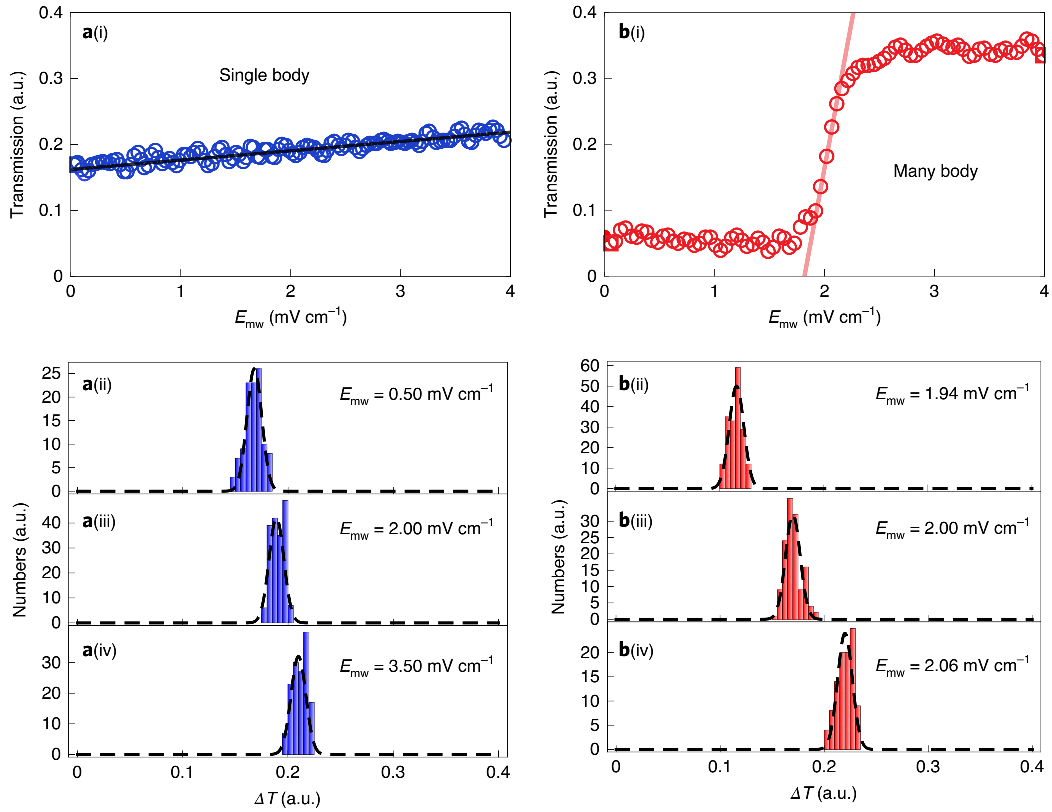

Fig. 5 | Transmission under different amplitudes of MW field. a,**b**, Data for the single-body (**a**(i)) and many-body (**b**(i)) case. The amplitude E_{mw} is changed from E_{mw} = 0 mV cm^{-1} to E_{mw} = 4 mV cm^{-1} in steps of 5 µs. The black and red solid lines are the fit linear functions $y = 0.014\,(x + 11.500)$ and $y = 0.890\,(x - 1.810)$, respectively. Here **a**(ii)–(iv) and **b** (ii)-(iv) are the critical-point histograms of the transmission distribution under different amplitudes of the MW field for the single and many-body case, respectively. The dashed lines are fitted Gaussian functions. The data are taken under equivalent experimental conditions (such as scan rate, acquisition time and averaging) in the few- and many-body cases.

number of excited and thus interacting Rydberg atoms but also depends on the measurement time t (ref. [37]), defined as the time the probe laser explores a small interval around each detuning Δ_s. In Fig. 3a–c, we consider the behaviour above criticality with $\Omega_p/2\pi$ = 7.9 MHz; in Fig. 3d–f, we consider the behaviour below criticality with $\Omega_p/2\pi$ = 5.5 MHz. We observe that for $\Omega_p/2\pi$ = 7.9 MHz, the transmission profile near the critical point becomes steeper as the measurement time t is increased, whereas for $\Omega_p/2\pi$ = 5.5 MHz, the transmission spectra are almost identical. This implies that the FI is inclined to be linearly dependent on the time t for the data in Fig. 3d–f, whereas a different dependence appears for the data in Fig. 3a–c.

The values of FI for different measurement times t are shown in Fig. 3g. We find that FI is well fitted by the form $F = A(t/t_0)^{\lambda}$, where $A = 2.0 \times 10^4$ MHz^{-2} and $\lambda = 1.28$ for $\Omega_p/2\pi$ = 7.9 MHz, whereas A = 10.0 MHz^{-2} and λ = 1.00 for $\Omega_p/2\pi$ = 5.5 MHz. In our system, when t = 1 ms, we achieve a large enhancement ratio of up to 10^3 by comparing these two cases. We conclude that one can extract more information by using an interacting many-body system than by independent systems, and that we can extract even more information by continuous measurements for long times. The non-integer power-law-dependent behaviour of the fit to the FI is caused by the critical slowing down and thus deviation of the atomic dynamics from the stationary state around the critical point[45–47]. This smooths the maximum slope and causes a more than linear suppression of the FI for shorter measurement times (Fig. 3a–c). We also plot the derivative $\mathrm{d}\bar{\mu}/\mathrm{d}\Delta_s$ against detuning Δ_s in the vicinity of critical detuning at t = 10 µs (Fig. 3b, inset). We find that the derivative $\mathrm{d}\bar{\mu}/\mathrm{d}\Delta$ has a power-law dependence on detuning, namely, $\mathrm{d}\bar{\mu}/\mathrm{d}\Delta_s = \chi|\Delta_s/\Delta_0 + 11.3|^{-\alpha}$, where χ = 0.02 MHz^{-1}, $\Delta_0/2\pi$ = 1 MHz and $\alpha = 2.0 \pm 0.1$ is the fitted power-law exponent. This detuning-dependent susceptibility is caused by the increased interaction near the critical point[48], as the change in detuning tunes the Rydberg population ρ_{rr} and hence the interaction. For the non-interacting case, the atomic system follows the stationary state even for the fast sweeps in our experiments, and the FI is linearly dependent on time t. There is more noise in Fig. 3c,f than Fig. 3a,d, due to low-frequency noises appearing for the longer measurement times.

Transmission spectra with and without MW fields

The advantages for metrology appear due to the critical response of the system on the variation in external perturbations. To further study this critical response, we apply an MW electric field with amplitude E_{mw} and detuning Δ_{mw} to continuously drive the Rydberg transition $51D_{3/2} - 52P_{1/2}$. The main effect of the MW field here is to (1) induce a small a.c. Stark shift that moves the critical point and (2) change the population of the Rydberg atoms, but it has a negligible effect on the C_6 van der Waals coefficient and resonant dipole–dipole interactions. As shown in Fig. 4a,b, this shifts the transmission spectra of the Rydberg system subject to the probe Rabi frequencies $\Omega_p/2\pi$ = 5.5 MHz and $\Omega_p/2\pi$ = 8.2 MHz, corresponding to the non-interacting and interacting many-body systems, respectively. When we apply the MW field with E_{mw} = 3.8 mV cm^{-1}, the spectra show a small redshift δ_s (Fig. 4a) and δ_m (Fig. 4b). For the many-body system, the high sensitivity of frequency shift allows us to sense the strength E_{mw} of an applied MW field. The FI ($F(\Delta)|_{\Delta_s=\Delta_c}$) for the black data in Fig. 4a is $F = 1.40 \times 10^{-3}$ MHz^{-2}, and is much smaller than that for the black data in Fig. 4b (F = 0.27 MHz^{-2}). The corresponding minimum uncertainty $\delta\Delta/2\pi \approx 0.3$ MHz corresponds to an uncertainty of the applied field ΔE_{mw} = 1.9 mV cm^{-1} by considering the energy shift proportional to E_{mw}^2 when E_{mw} is small (here the stark shift $\delta_m \approx E^2_{mw}$ follows a Taylor expansion, namely, $\delta_m \approx -\Delta_{mw}/2 + \sqrt{\Delta^2_{mw} + \Omega^2_{mw}}/2)$ (Supplementary Fig. 3). As a result, the many-body system can directly sense the strength $E_{mw} = 3.8$ mV cm^{-1} by measuring the spectrum shift ($\delta_m = 2\pi \times 1.2(0.3)$ MHz). In comparison, the spectral shift δ_s is indistinguishable for independent atoms, which are, thus, not sensitive enough to sense the same MW field by monitoring the spectral shift.

Optical response under electric fields with different amplitudes
The many-body metrological ruler has a thinner tick mark and thus better precision than the single-body ruler, because the optical response is stronger in the many-body case when subject to a small frequency shift. We can also measure the optical transmission at the position of the steepest slope $p_{\omega 1}$ (Fig. 1b) when the atoms are subject to an MW electric field $E_{mw}\sin(f_0 t)$, where $f_0/2\pi = 16.60$ GHz is near resonant with the radio-frequency (RF) transition $51D_{3/2} \leftrightarrow 52P_{1/2}$.

We measure the transmission when increasing the amplitude of the MW with detuning Δ_s fixed near the maximum slope under the many- and single-body conditions (Fig. 5a,b, respectively). For the single-body condition, the transmission is not sensitive to the variance in amplitude E_{mw}. For the many-body condition, the change in E_{mw} makes the system cross the critical point and the transmission signal is highly sensitive to the field around values of $E_{mw} = 2$ mV cm^{-1} (this position can be tuned by coupling detuning) (Fig. 5b). To evaluate the sensitivity, we fit the data near criticality with a linear function $y = k(x + x_0)$ ($k = \overline{\mu}'(E_{mw})$), and obtain the ratio of the slopes $k_2/k_1 = 63.57$, where k_1 and k_2 represent the linear coefficients for the single- and many-body cases, respectively. Since the variance Var(μ) is almost the same for these two cases (Fig. 5a(ii)–(iv),b(ii)–(iv)), we can obtain an enhanced ratio for the FI: $(k_2^2/\mathrm{Var}(\mu))/(k_1^2/\mathrm{Var}(\mu)) > 4000$From the E_{mw}-dependent transmission, we can distinguish the standard deviation of the amplitude $\delta E_{mw} = 1.4$ mV cm^{-1} for the non-interacting case and $\delta E_{mw} = 22$ µV cm^{-1} for the interacting many-body case with data acquisition time of 5 µs per data point. By considering multiple sequential independent measurements, we estimate the equivalent sensitivity to be 49 nV cm^{-1} Hz$^{-1/2}$.

Discussion
Although previous work[12] clearly shows effects sensitive to the electric field, that work mainly elaborated on how the presence of ionized Rydberg atoms induce a linear shift in the critical point. In contrast, the critical behaviour of the interacting many-body system has not been previously employed for sensing. The criticality induced by the interacting Rydberg atoms depends on the Rydberg atom number N and interaction strength V (ref. [8]), and the increase in population ρ_{rr} or interaction strength $V\rho_{rr}$ enhances the nonlinearity of criticality. In our system, we have a large interacting number of atoms, and the energy splitting is far from the one of N isolated systems[31–36]. Specifically, the interaction-induced nonlinear FI dependence on the measurement time of a single frequency scan shows a unique advantage on sensing, which agrees with theoretical simulations (Supplementary Fig. 1).

In summary, we have demonstrated the critical behaviour of interacting Rydberg atoms and characterized its metrological consequences. The FI for the estimation of a weak MW field shows an enhancement of the order of 10^3 by the use of interacting many-body systems. Concerning the use of FI and Cramér–Rao bound, we note that not only the narrow detuning interval with the highest slope but the entire transmission signal contributes in an integral manner to the sensitivity of experiments (a similar analysis of spatial image processing is provided elsewhere[49,50]). Our analysis captures the main contribution to that integral and thus constitutes a lower limit to the FI. Passing from the measurement of frequencies, the experiments derive their improved sensitivity towards MW electric fields and show that the Rydberg non-equilibrium system can act as a versatile high-sensitivity metrological resource.

Online content
Any methods, additional references, Nature Research reporting summaries, source data, extended data, supplementary information, acknowledgements, peer review information; details of author contributions and competing interests; and statements of data and code availability are available at https://doi.org/10.1038/s41567-022-01777-8.

References

1. Greiner, M., Mandel, O., Esslinger, T., Hänsch, T. W. & Bloch, I. Quantum phase transition from a superfluid to a Mott insulator in a gas of ultracold atoms. *Nature* **415**, 39–44 (2002).
2. Bernien, H. et al. Probing many-body dynamics on a 51-atom quantum simulator. *Nature* **551**, 579–584 (2017).
3. Martin, M. J. et al. A quantum many-body spin system in an optical lattice clock. *Science* **341**, 632–636 (2013).
4. Colombo, S., Pedrozo-Peñafiel, E., Adiyatullin, A.F. et al. Time-reversal-based quantum metrology with many-body entangled states. *Nat. Phys.* **18**, 925–930. https://doi.org/10.1038/s41567-022-01653-5 (2022).
5. Lukin, M. D. et al. Dipole blockade and quantum information processing in mesoscopic atomic ensembles. *Phys. Rev. Lett.* **87**, 037901 (2001).
6. Saffman, M., Walker, T. G. & Mølmer, K. Quantum information with Rydberg atoms. *Rev. Mod. Phys.* **82**, 2313 (2010).
7. Carr, C., Ritter, R., Wade, C. G., Adams, C. S. & Weatherill, K. J. Nonequilibrium phase transition in a dilute Rydberg ensemble. *Phys. Rev. Lett.* **111**, 113901 (2013).
8. Ding, Dong-Sheng, Busche, H., Shi, Bao-Sen, Guo, Guang-Can & Adams, C. S. Phase diagram of non-equilibrium phase transition in a strongly-interacting Rydberg atom vapour. *Phys. Rev. X* **10**, 021023 (2020).
9. Malossi, N. et al. Full counting statistics and phase diagram of a dissipative Rydberg gas. *Phys. Rev. Lett.* **113**, 023006 (2014).
10. de Melo, N. R. et al. Intrinsic optical bistability in a strongly driven Rydberg ensemble. *Phys. Rev. A.* **93**, 063863 (2016).
11. Šibalić, N., Wade, C. G., Adams, C. S., Weatherill, K. J. & Pohl, T. Driven-dissipative many-body systems with mixed power-law interactions: bistabilities and temperature-driven nonequilibrium phase transitions. *Phys. Rev. A.* **94**, 011401 (2016).
12. Wade, C. G. et al. A terahertz-driven non-equilibrium phase transition in a room temperature atomic vapour. *Nat. Commun.* **9**, 3567 (2018).
13. Wintermantel, T. M. et al. Epidemic growth and Griffiths effects on an emergent network of excited atoms. *Nat. Commun.* **12**, 103 (2020).
14. Ding, D.-S. et al. Epidemic spreading and herd immunity in a driven non-equilibrium system of strongly-interacting atoms. Preprint at https://arxiv.org/abs/2106.12290 (2021).
15. Gibbs, H. M., McCall, S. L. & Venkatesan, T. N. C. Differential gain and bistability using a sodium-filled Fabry-Perot interferometer. *Phys. Rev. Lett.* **36**, 1135 (1976).
16. Wang, H., Goorskey, D. J. & Xiao, M. Bistability and instability of three-level atoms inside an optical cavity. *Phys. Rev. A.* **65**, 011801 (2001).
17. Wang, H., Goorskey, D. & Xiao, M. Enhanced Kerr nonlinearity via atomic coherence in a three-level atomic system. *Phys. Rev. Lett.* **87**, 073601 (2001).
18. Pickup, L. et al. Optical bistability under nonresonant excitation in spinor polariton condensates. *Phys. Rev. Lett.* **120**, 225301 (2018).
19. Hehlen, M. P. et al. Cooperative bistability in dense, excited atomic systems. *Phys. Rev. Lett.* **73**, 1103 (1994).
20. Lee, T. E., Haeffner, H. & Cross, M. C. Collective quantum jumps of Rydberg atoms. *Phys. Rev. Lett.* **108**, 023602 (2012).

21. Marcuzzi, M., Levi, E., Diehl, S., Garrahan, J. P. & Lesanovsky, I. Universal nonequilibrium properties of dissipative Rydberg gases. *Phys. Rev. Lett.* **113**, 210401 (2014).
22. Weimer, H. Variational principle for steady states of dissipative quantum many-body systems. *Phys. Rev. Lett.* **114**, 040402 (2015).
23. Levi, E., Gutiérrez, R. & Lesanovsky, I. Quantum non-equilibrium dynamics of Rydberg gases in the presence of dephasing noise of different strengths. *J. Phys. B: At. Mol. Opt. Phys.* **49**, 184003 (2016).
24. Fan, H. et al. Atom based RF electric field sensing. *J. Phys. B: At. Mol. Opt. Phys.* **48**, 202001 (2015).
25. Sedlacek, J. A. et al. Microwave electrometry with Rydberg atoms in a vapour cell using bright atomic resonances. *Nat. Phys.* **8**, 819–824 (2012).
26. Facon, A. et al. A sensitive electrometer based on a Rydberg atom in a Schrödinger-cat state. *Nature* **535**, 262–265 (2016).
27. Cox, K. C., Meyer, D. H., Fatemi, F. K. & Kunz, P. D. Quantum-limited atomic receiver in the electrically small regime. *Phys. Rev. Lett.* **121**, 110502 (2018).
28. Jing, M. et al. Atomic superheterodyne receiver based on microwave-dressed Rydberg spectroscopy. *Nat. Phys.* **16**, 911–915 (2020).
29. Liu, Zong-Kai et al. Deep learning enhanced Rydberg multifrequency microwave recognition. *Nat. Commun.* **13**, 1997 (2022).
30. Gammelmark, S. & Mølmer, K. Phase transitions and Heisenberg limited metrology in an Ising chain interacting with a single-mode cavity field. *New J. Phys.* **13**, 053035 (2011).
31. Macieszczak, K., Guţă, M., Lesanovsky, I. & Garrahan, J. P. Dynamical phase transitions as a resource for quantum enhanced metrology. *Phys. Rev. A* **93**, 022103 (2016).
32. Fernández-Lorenzo, S. & Porras, D. Quantum sensing close to a dissipative phase transition: symmetry breaking and criticality as metrological resources. *Phys. Rev. A* **96**, 013817 (2017).
33. Raghunandan, M., Wrachtrup, J. örg & Weimer, H. High-density quantum sensing with dissipative first order transitions. *Phys. Rev. Lett.* **120**, 150501 (2018).
34. Garbe, L., Bina, M., Keller, A., Paris, MatteoG. A. & Felicetti, S. Critical quantum metrology with a finite-component quantum phase transition. *Phys. Rev. Lett.* **124**, 120504 (2020).
35. Chu, Y., Zhang, S., Yu, B. & Cai, J. Dynamic framework for criticality-enhanced quantum sensing. *Phys. Rev. Lett.* **126**, 010502 (2021).
36. Montenegro, V., Mishra, U. & Bayat, A. Global sensing and its impact for quantum many-body probes with criticality. *Phys. Rev. Lett.* **126**, 200501 (2021).
37. Ilias, T., Yang, D., Huelga, S. F. & Plenio, M. B. Criticality enhanced quantum sensing via continuous measurement. PRX Quantum 3, 010354. 10.1103/PRXQuantum.3.010354 (2022).
38. Garbe, L., Abah, O., Felicetti, S. & Puebla, R. Critical quantum metrology with fully-connected models: from Heisenberg to Kibble-Zurek scaling. Quantum Sci. Technol. 7 035010 https://doi.org/10.1088/2058-9565/ac6ca5 (2022).
39. Liu, R. et al. Experimental critical quantum metrology with the Heisenberg scaling. *npj Quantum Inf.* **7**, 170 (2021).
40. Zanardi, P., Paris, MatteoG. A. & Campos Venuti, L. Quantum criticality as a resource for quantum estimation. *Phys. Rev. A* **78**, 042105 (2008).
41. Rossini, D. & Vicari, E. Dynamic Kibble-Zurek scaling framework for open dissipative many-body systems crossing quantum transitions. *Phys. Rev. Res.* **2**, 023211 (2020).
42. Pelissetto, A., Rossini, D. & Vicari, E. Dynamic finite-size scaling after a quench at quantum transitions. *Phys. Rev. E* **97**, 052148 (2018).
43. Pezzè, L., Smerzi, A., Oberthaler, M. K., Schmied, R. & Treutlein, P. Quantum metrology with nonclassical states of atomic ensembles. *Rev. Mod. Phys.* **90**, 035005 (2018).
44. Braunstein, S. L., Caves, C. M. & Milburn, G. J. Generalized uncertainty relations: theory, examples, and Lorentz invariance. *Ann. Phys.* **247**, 135–173 (1996).
45. Zurek, W. H., Dorner, U. & Zoller, P. Dynamics of a quantum phase transition. *Phys. Rev. Lett.* **95**, 105701 (2005).
46. Clark, L. W., Feng, L. & Chin, C. Universal space-time scaling symmetry in the dynamics of bosons across a quantum phase transition. *Science* **354**, 606–610 (2016).
47. Keesling, A. et al. Quantum Kibble–Zurek mechanism and critical dynamics on a programmable Rydberg simulator. *Nature* **568**, 207–211 (2019).
48. Trenkwalder, A. et al. Quantum phase transitions with parity-symmetry breaking and hysteresis. *Nat. Phys.* **12**, 826–829 (2016).
49. Negretti, A., Henkel, C. & Mølmer, K. Quantum-limited position measurements of a dark matter-wave soliton. *Phys. Rev. A* **77**, 043606 (2008).
50. Delaubert, V., Treps, N., Fabre, C., Bachor, H. A. & Réfrégier, P. Quantum limits in image processing. *EPL* **81**, 44001 (2008).

https://doi.org/10.1038/s41567-022-01777-8

Methods

Experimental setup

We adopt a two-photon transition scheme to excite an atomic ground state to a Rydberg state, using a probe field resonantly driving the atomic transition $5S_{1/2}$, $F = 2 \to 5P_{1/2}$, $F'=3$, and a coupling field driving the transition $5P_{1/2}$, $F'=3 \to 51D_{3/2}$. An MW electric field 1 (or 2) may be applied to drive an RF transition between two different Rydberg states $51D_{3/2}$ and $52P_{1/2}$ (or $50F_{5/2}$). The MW electric fields used in our experiment are generated by two RF sources and two frequency horns. A 795 nm laser is split by a beam displacer into a probe beam and identical reference beam, which are both propagating in parallel through a heated Rb cell (length, 10 cm). The temperature is set as 44.6 °C, corresponding to the atomic density of 9.0×10^{10} cm^{-3}. One probe beam is overlapped with a counterpropagating coupling beam to constitute the Rydberg electromagnetically induced transparency process. The two transmission signals are detected on a differencing photodetector.

Generation and calibration of MW fields

The MW fields used in our experiment are generated by two RF sources and two frequency horns. The first RF source works in the range from d.c. to 40 GHz and the other, from d.c. to 20 GHz. The frequency horns are set close to the Rb cell. The RF frequency between Rydberg D and P/F states are calculated according to the algorithm mentioned elsewhere[51]. We use a spectrum analyser (Ceyear 4024f, ~9 kHz to 32 GHz) and an antenna (~380 MHz to 20 GHz) to receive the MW fields and then to calibrate the amplitude of MW fields in the centre of the Rb cell.

FI and Cramér–Rao bound

In parameter estimation, the Cramér–Rao bound sets a lower limit to the statistical estimation error by ν independent experiments, that is, $(\delta\theta)_{\min} = 1/\sqrt{\nu \times F(\theta)}$. Here $F(\theta)$ is the FI with value

$$F(\theta) = \sum_{\mu} \frac{1}{L(\mu,\theta)}\left(\frac{\partial L(\mu,\theta)}{\partial\theta}\right)^2, \tag{6}$$

where $L(\mu, \theta)$ is the likelihood function for the possible measurement outcome μ, conditioned on parameter θ (ref. [52]).

In our experiment, we subtract two counting signals that may both be well described by Poisson distributions with mean values $\bar{\mu}_1$ and $\bar{\mu}_2$, and the same values for their variances. Both count numbers are large; in our experiments, the observed noise is dominated by electronic noise, and hence, both distributions are well approximated by Gaussian distributions. The difference signal is, thus, described by a Gaussian distribution with mean value $\bar{\mu} = \bar{\mu}_1 - \bar{\mu}_2$ and variance $\sigma^2 = \bar{\mu}_1 + \bar{\mu}_2$. For a Gaussian distribution with the likelihood[53,54]

$$L(\mu,\theta) = \frac{1}{\sqrt{2\pi\sigma^2}} e^{-\frac{1}{2}\left(\frac{\mu-\bar{\mu}(\theta)}{\sigma}\right)^2}, \tag{7}$$

one can see that

$$\frac{\partial L(\mu,\theta)}{\partial\theta} = \left(\frac{\mu-\bar{\mu}}{\sigma^2}\right) L(\mu,\theta)\bar{\mu}'(\theta). \tag{8}$$

We, hence, obtain

$$\begin{aligned} F(\theta) &= \sum_{\mu} \frac{1}{L(\mu,\theta)}\left(\left(\frac{\mu-\bar{\mu}}{\sigma^2}\right)L(\mu,\theta)\bar{\mu}'(\theta)\right)^2 \\ &= \sum_{\mu} L(\mu,\theta)\frac{(\mu-\bar{\mu})^2}{\sigma^4}\left(\bar{\mu}'(\theta)\right)^2 \\ &= \frac{\mathrm{Var}(\mu)}{\sigma^4}\left(\bar{\mu}'(\theta)\right)^2 = \frac{\left(\bar{\mu}'(\theta)\right)^2}{\sigma^2} \end{aligned}, \tag{9}$$

where $\bar{\mu}'(\theta)$ denotes the derivative of mean $\bar{\mu}(\theta)$ with respect to θ. There is further contribution to FI due to the dependence of variance σ^2 on θ. Its value is $\frac{1}{2\sigma^4}\left(\frac{\mathrm{d}(\sigma^2)}{\mathrm{d}\theta}\right)^2$; for our system, it plays a less important role.

Signal-to-noise ratio analysis

For a given Gaussian incident probe and reference beams with mean photon signal μ_0 in one second, the on-resonance absorption coefficient of the atoms and loss of optical path is $1-\zeta$ (corresponding to transmission ratio ζ), a differencing photodetector with efficiency η records a Poisson-distributed number of clicks with mean value $\eta\mu_0$ and variance $\eta\mu_0$ per second, which outputs a voltage signal. The difference between the two beams is much weaker and has the mean value of

$$\mu = \zeta\eta\mu_0[1+\varepsilon(\Delta_s)]t - \zeta\eta\mu_0 t = \zeta\eta\mu_0\varepsilon(\Delta_s)t, \tag{10}$$

where $\varepsilon(\Delta_s)$ is the transmission probability induced by the Rydberg electromagnetically induced transparency effect and t is the considered time interval. As the input photon number of each beam is very large, namely, $\mu_0 \approx 10^{14}$ photons per second for $\Omega_p/2\pi = 7.9$ MHz, the variance of the difference in the two beams per second is the sum of the means because the difference in two Gaussian-distributed variables is also a Gaussian-distributed variable: $\mathrm{Var}(\mu) = 2\zeta\eta\mu_0 + \zeta\eta\mu_0\varepsilon(\Delta_s) \approx 2\zeta\eta\mu_0$, where $\zeta = 20.6\%$ for $\Omega_p/2\pi = 7.9$ MHz, $\zeta = 14.6\%$ for $\Omega_p/2\pi = 6.5$ MHz and $\zeta = 8.7\%$ for $\Omega_p/2\pi = 5.5$ MHz. The output voltage signal of the differencing photodetector could be converted into the photon number by a voltage conversion ratio of $G = 5.3 \times 10^7$ V W^{-1}. Half of the voltage output signal corresponds to ~1×10^{10} photon numbers per second. The coupling detuning Δ_s is swept with rate υ_s and sampling rate M (means that there are an average of M data points in the swept detuning Δ_s), the transmission spectrum could be measured by accumulating the photon numbers in each detuning interval. A fast scan accumulates small photon numbers for each interval, whereas a slow scan achieves large photon numbers. If we scan the detuning of coupling laser Δ_s from red to blue detuning and vice versa, we could observe bistability[7,8,55]. The bistability shifted by the MW fields is provided in Supplementary Fig. 2.

Nonlinearity of interacting atoms

To elucidate the sensitivity of Rydberg atoms to frequency for different interaction strengths, we consider a two-level atom model with ground state $|g\rangle$ and Rydberg state $|r\rangle$ (with spontaneous radiation rate Γ), which are coupled by a laser with Rabi frequency Ω and detuning from resonance Δ. After mean-field approximation (that is, $\Delta \to \Delta - V\rho_{rr}$, where V is the many-body interaction term from dipole interaction or ion collisions and ρ_{rr} is the population of Rydberg state), the steady-state solution for a two-level optical Bloch equation is[20]

$$\begin{aligned} \dot{\rho}_{gr} &= \mathrm{i}\frac{\Omega}{2}(\rho_{rr}-\rho_{gg}) + \mathrm{i}\Delta_{\mathrm{eff}}\rho_{gr} - \frac{\Gamma}{2}\rho_{gr} \\ \dot{\rho}_{rr} &= -\mathrm{i}\Omega(\rho_{gr}-\rho_{rg}) - \Gamma\rho_{rr} \end{aligned}, \tag{11}$$

where Δ_{eff} is the effective detuning $\Delta_{\mathrm{eff}} = \Delta - V\rho_{rr}$ by considering an interaction strength V. We obtain an equation about ρ_{rr} for bistability as follows:

$$V^2\rho_{rr}^3 - 2V\Delta\rho_{rr}^2 + \left(\Delta^2 + \Omega^2/2 + \Gamma^2/4\right)\rho_{rr} - \Omega^2/4 = 0. \tag{12}$$

By taking the derivative of both sides, we finally get the relationship between the slope of the steep edge of the hysteresis loop $\max(\mathrm{d}\rho_{rr}/\mathrm{d}\Delta)$ and the interaction of Rydberg atoms V.

$$\frac{\mathrm{d}\rho_{rr}}{\mathrm{d}\Delta} = -\frac{8\left(\Delta\rho_{rr} - \rho_{rr}^2 V\right)}{\Gamma^2 + 4\Delta^2 + 12\rho_{rr}^2V^2 - 16\Delta\rho_{rr}V + 2\Omega^2} \tag{13}$$

The critical point is defined when this derivative reaches infinity, that is, $\mathrm{d}\rho_{rr}/\mathrm{d}\Delta \Rightarrow \infty$, from which the threshold of the Rydberg population

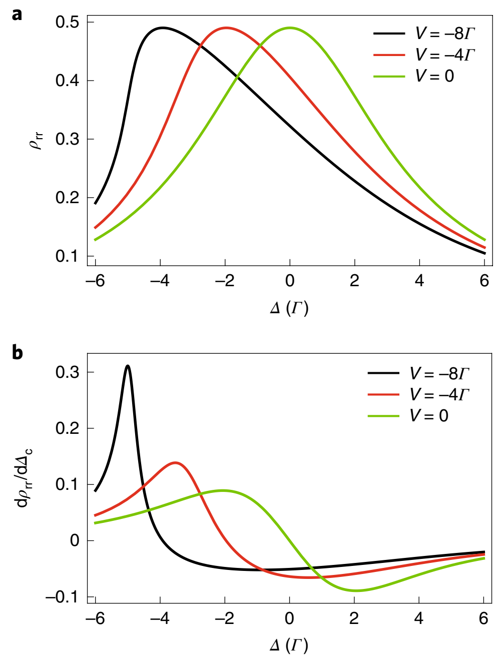

Fig. 6 | Theoretical simulations of interacting two-level atoms. a, Rydberg state population ρ_{rr} as a function of laser detuning Δ for different interaction strengths V. **b**, Derivative of Rydberg population with respect to Δ.

is obtained, that is,

$$\rho_{th} = \frac{\sqrt{-3\Gamma^2V^2 + 4\Delta^2V^2 - 6V^2\Omega^2} + 4\Delta V}{6V^2}. \quad (14)$$

The relation between ρ_{rr}, $d\rho_{rr}/d\Delta$ and Δ is demonstrated in Fig. 6. By letting the derivative equal to 0, that is, $d\rho_{rr}/d\Delta = 0$, we obtain the analytical expression of the maximum derivative $d\rho_{rr}/d\Delta|_{\Delta=\Delta_c}$ and the corresponding detuning Δ_c as follows:

$$\Delta_c = \frac{1}{6}\left(6\rho_{rr}V - \sqrt{3}\sqrt{\Gamma^2 + 2\Omega^2}\right), \quad (15)$$

$$\frac{d\rho_{rr}}{d\Delta}(\Delta_c) = \frac{1}{V + \sqrt{(\Gamma^2 + 2\Omega^2)/3\rho_{rr}^2}}. \quad (16)$$

Data availability

The data that support this study are available via GitHub[56] at https://github.com/ZongkaiLiu/many-body-enhanced-metrology. Source data are provided with this paper.

References

51. Šibalić, N., Pritchard, J. D., Adams, C. S. & Weatherill, K. J. ARC: an open-source library for calculating properties of alkali Rydberg atoms. *Comput. Phys. Commun.* **220**, 319–331 (2017).
52. Lehmann, E. L. & Casella, G. *Theory of Point Estimation* (Springer, 1998).
53. Mardia, K. V. & Marshall, R. J. Maximum likelihood estimation of models for residual covariance in spatial regression. *Biometrika* **71**, 135–146 (1984).
54. Miller, K. S. *Complex Stochastic Processes: An Introduction to Theory and Application* (Addison Wesley Publishing Company, 1974).
55. Weller, D., Urvoy, A., Rico, A., Löw, R. & Kübler, H. Charge-induced optical bistability in thermal Rydberg vapor. *Phys. Rev. A.* **94**, 063820 (2016).
56. Zong-Kai, L. Original data for 'Enhanced metrology at the critical point of a many-body Rydberg atomic system'. *GitHub* https://github.com/ZongkaiLiu/many-body-enhanced-metrology (2022).

Acknowledgements

D.-S.D. thanks the discussions with J. Ye (JILA). Z.-K.L. appreciates the instructive discussions with T.-Y. Xie. D.-S.D. acknowledges funding from the National Key Research and Development Program of China (2017YFA0304800), the National Natural Science Foundation of China (grant no. U20A20218), the Major Science and Technology Projects in Anhui Province (grant no. 202203a13010001) and the Youth Innovation Promotion Association of the Chinese Academy of Sciences under grant no. 2018490. B.-S.S. acknowledges funding from the National Natural Science Foundation of China (grant no. 11934013), the Innovation Program for Quantum Science and Technology (2021ZD0301100) and Anhui Initiative in Quantum Information Technologies (AHY020200). C.-S.A. acknowledges funding from the EPSRC through grant agreements EP/M014398/1 ('Rydberg Soft Matter'), EP/R002061/1 ('Atom-based Quantum Photonics'), EP/L023024/1 ('Cooperative Quantum Optics in Dense Thermal Vapours'), EP/P012000/1 ('Solid State Superatoms'), EP/R035482/1 ('Optical Clock Arrays for Quantum Metrology') and EP/S015973/1 ('Microwave and Terahertz Field Sensing and Imaging using Rydberg Atoms'); the Danish National Research Foundation through the Center of Excellence for Complex Quantum Systems (grant agreement no. DNRF156); DSTL; and Durham University.

Author contributions

D.-S.D. conceived the idea and implemented the physical experiments with Z.-K.L. Z.-K.L., D.-S.D. and K.M. employed the FI. D.-S.D., Z.-K.L. and K.M. derived the equations, plotted the figures and wrote the manuscript. All the authors contributed to the discussions regarding the results and analysis contained in the manuscript. D.-S.D., B.-S.S., G.-C.G. and C.-S.A. sponsor this project.

Competing interests

The authors declare no competing interests.

Additional information

Supplementary information The online version contains supplementary material available at https://doi.org/10.1038/s41567-022-01777-8.

Correspondence and requests for materials should be addressed to Dong-Sheng Ding, Bao-Sen Shi, Klaus Mølmer or Charles S. Adams.

Peer review information *Nature Physics* thanks Shannon Whitlock and Abolfazl Bayat for their contribution to the peer review of this work.